PAPER

Eu^{3+} activated BaF$_2$ nanostructured thin films: fabrication and a combined experimental and computational study of the energy conversion process†

Francesca Lo Presti, [ID] [a] Anna Lucia Pellegrino,[a] Emil Milan, [ID] [b] Eros Radicchi, [ID] [b] Adolfo Speghini [ID] *[b] and Graziella Malandrino [ID] *[a]

Significant work has recently focused on developing novel materials suitable for solar technologies with better conversion efficiencies, while maintaining low costs. BaF$_2$ has been investigated as a fluoride host for doping with luminescent ions for energy conversion processes in photovoltaic cells. This work employed a metal–organic chemical vapor deposition technique to prepare nanostructured europium-doped BaF$_2$ thin films on silicon and quartz substrates. Samples have been fabricated by varying the deposition temperature from 300 to 600 °C in order to examine how temperature affects the structure, morphology, and luminescence of Eu-doped BaF$_2$ thin films. A multicomponent combination of fluorinated β-diketonate metal–organic precursors of barium and europium, Ba(hfa)$_2$·tetraglyme and Eu(hfa)$_3$·diglyme, in an appropriate molar ratio, is employed to fabricate BaF$_2$ based thin films. These precursors serve as a single molten source by delivering all the elements required (Ba, Eu, and F) for forming the Eu-doped BaF$_2$ phase due to the similar nature of the ligands. On silicon substrates, preliminary deposition tests have been carried out to confirm the purity, homogeneity, and appropriate stoichiometry of films. The obtained results pave the way for the production of BaF$_2$ thin films doped with lanthanide ions, particularly interesting for their up-conversion (UC), down-conversion (DC), and down-shifting (DS) properties.

Introduction

Nowadays, scientific research is playing a crucial role in renewable and sustainable energy fields and many efforts have been devoted to upcoming innovations in the photovoltaic industry. Among the numerous materials with photovoltaic (PV) applications, only a few of them can ensure a high conversion efficiency of solar radiation, which appears to be at least greater than 20%.[1] Therefore, only a fraction of solar radiation that reaches PV cells is converted into electrical energy. One of the reasons for this low efficiency concerns the capability of photon collection by the active material, which is related to its bandgap characteristics. In the present time, silicon-based solar cells are able to achieve efficiencies of up to 26.7%.[2] An innovative approach, tested to enhance the efficiency of PV systems, is based on the conversion of photons whose energies do not match the bandgap of the active material (usually silicon) into an appropriate energetic range. The energy conversion (EC) process can be achieved by integrating, in the PV panel, a material able to host an active luminescent species,[3] giving rise to up-conversion, down-conversion or down-shifting processes. In up-conversion (UC) processes, photons with energies generally in the near-infrared (NIR) region are converted into higher energy photons, typically in the ultraviolet (UV) or visible range. The down-conversion (DC) process, also known as "quantum cutting", is based on the process in which one high energy photon in the UV region is usually converted into two photons of lower energy in the visible range. On the other hand, down-shifting (DS) is the process where high energy photons, often in the UV region, are absorbed by a photoluminescent substance and then released as lower energy photons.[4,5] Thus, the insertion of a down-shifting film in a photovoltaic cell would allow the exploitation of UV photons typically unused by the active layer, by converting them into visible, absorbable photons.

The choice of the host material plays a crucial role in the DS process: it must be highly crystalline because the potential

[a] *Dipartimento di Scienze Chimiche, Università di Catania, and INSTM UdR Catania, Viale A. Doria 6, I-95125 Catania, Italy. E-mail: gmalandrino@unict.it*

[b] *Nanomaterials Research Group, Department of Biotechnology, University of Verona and INSTM RU Verona, Strada Le Grazie 15, I-37134 Verona, Italy. E-mail: adolfo.speghini@univr.it*

† Electronic supplementary information (ESI) available. See DOI: https://doi.org/10.1039/d3tc02666c

This journal is © The Royal Society of Chemistry 2023

J. Mater. Chem. C, 2023, **11**, 12195–12205 | **12195**

presence of defects within the host structure may in principle decrease the radiative emission pathways of the activator ion due to non-radiative deexcitation.[6] Furthermore, the choice of the correct lanthanide (Ln^{3+}) ion depends on several factors, especially on high emission efficiency and long lifetimes. In fact, due to the forbidden nature of their 4f–4f intra-configurational transitions, the lanthanide ion emissions show long decay times (micro- or even milliseconds), increasing the chances of sequential excitations and energy transfers populating the excited energy levels.[7]

Eu^{3+} ions have attracted great attention from the scientific community, thanks to the long decay times of the mainly emitting $^5D_0$ excited state, related to the typical red emission at around 615 nm, making it attractive for applications in nanothermometry,[8] biomedicine,[9] and, recently, also in photo-voltaics as a luminescent dopant in inorganic matrices for DC processes.[10,11]

Actually, it has been demonstrated that fluoride hosts, compared to other inorganic ones, such as metal oxides, are more efficient for energy conversion processes.[12] Specifically, ternary (i.e. $NaYF_4$ and $NaGdF_4$)[13–18] and alkaline-earth binary fluorides (i.e. CaF_2, SrF_2 and BaF_2)[19–23] are considered among the most efficient hosts for the UC, DC and DS luminescence of Ln^{3+} ions.

BaF_2 has been investigated as a fluoride host for EC processes due to its low phonon energy, high optical transparency (from 150 nm to 15 μm), exceptional chemical stability and versatile synthetic strategies.[24,25] To date all literature reports on the luminescence properties of Eu^{3+} doped BaF_2 refer to nanocrystals[26] and nanoparticles.[27,28] Only one report describes the fabrication of epitaxial Eu-doped BaF_2 thin films deposited through the molecular beam epitaxy (MBE) technique,[29] and recently Neizvestny et al. have synthesized high epitaxial BaF_2 films through MBE.[30]

Very few studies have been reported for the deposition of pure BaF_2 and Eu-doped BaF_2 in the form of thin films.[29–34] Nevertheless, nanostructured thin films, fabricated through a low-cost, efficient and easily scalable route, are highly required to fabricate a downshifting layer in a photovoltaic cell.

In this context, metal–organic chemical vapor deposition (MOCVD) is a quite appealing technique for the deposition of thin films and is widely used both in scientific and industrial fields thanks to its various advantages that include simplified instrumental equipment, high deposition rate, deposition of uniform films on large areas, straightforward tuning of the doping amount and easy industrial scale-up. To date, very few reports have described the deposition of BaF_2 thin films through an MOCVD approach.[31–34]

Hence, the aim of this study concerns an in-depth study on the MOCVD fabrication of Eu^{3+} doped BaF_2 thin films, focusing attention on the fabrication process and the luminescence properties. This study represents, to our knowledge, the first case of Eu-doped BaF_2 fabrication by MOCVD. For the formation of BaF_2 doped with Eu^{3+} ions, a multicomponent mixture of second generation β-diketonate fluorinated precursors has been considered, i.e. $Ba(hfa)_2$·tetraglyme and $Eu(hfa)_3$·diglyme, mixed together to act as a single-molten source. The deposited films have been characterized using several techniques for a thorough structural, morphological, and compositional analysis. The DS luminescent properties have been investigated and the corresponding energy levels of Eu^{3+} are compared with results obtained from ab initio molecular simulations.

Experimental

Materials

Barium hydroxide octahydrate (purity 98 + %), europium(III) acetate hydrate (purity 99.9%), and β-diketone (Hhfa) (purity 98%) were purchased from STREM Chemicals, while diglyme (purity 99.5%) and tetraglyme (purity 99.9%) were purchased from Sigma Aldrich, and used without further purification processes. $Ba(hfa)_2$·tetraglyme and $Eu(hfa)_3$·diglyme complexes were synthesized by reacting Ba hydroxide or Eu acetate with Hhfa and a polyether such as tetraglyme or diglyme, respectively. The synthesis was carried out, according to the literature, in dichloromethane under reflux for 1 h.[35,36]

Film syntheses

For the MOCVD deposition of pure and Eu-doped BaF_2 thin films, a customized, horizontal, hot-wall reactor was used (Fig. S1, ESI†). A multicomponent mixture of "second generation" β-diketonate precursors in different molar ratios was used as a single molten source. The mixture of $Ba(hfa)_2$·tetraglyme and $Eu(hfa)_3$·diglyme precursors with Ba:Eu ratios of 0.99:0.01, 0.90:0.10 and 0.80:0.20 have been used to produce BaF_2 films doped at 1%, 10% or 20%, respectively. The mixture was heated at 160 °C, a suitable temperature for its effective vaporization without thermal degradation. The depositions were carried out for 60 minutes in a horizontal hot-wall reactor at reduced pressure (4 Torr). Deposition temperature was varied in the range from 300 to 600 °C. A flow of argon (150 sccm) was used as the carrier gas and a flow of oxygen (150 sccm) was used as the reactant gas, which was introduced in the main flow in proximity to the reaction zone. The films were deposited on Si (100) and quartz substrates which were introduced into the reactor and coated simultaneously.

Film characterization

The BaF_2:Eu films were analyzed using an XRD Smartlab Rigaku diffractometer in the grazing incidence mode (0.5°) operating with a rotating anode of the Cu K_α source radiation at 45 kV and 200 mA. The diffraction peaks were compared with those present in the Powder Data File database, and a triplet of Miller indices was associated with each peak. The morphology of the deposited films was investigated using a field emission scanning electron microscope (FE-SEM) ZEISS SUPRA 55 VP. The atomic composition of the films was obtained by using an energy dispersive X-Ray (EDX) system, with an INCA-Oxford windowless detector and a resolution of 127 eV calculated as full width half maximum (FWHM) of K_α of Mn.

Luminescence investigation

The Eu^{3+} doped BaF$_2$ films were excited with a LED flashlight centered at 385 nm, and the emission spectra were recorded at 90° geometry with a 4× microscope objective. A band pass filter centered at 390 nm was used to filter the excitation radiation and a cutoff filter at 532 nm was used to reject the scattered excitation radiation. The emission spectra were obtained using a Czerny–Turner monochromator (Andor Shamrock 500i) equipped with a 300 lines per mm grating (resolution 1.27 nm) and an iDus CCD camera cooled to −90 °C. The excitation spectra were recorded using a Fluorolog-3 (Horiba-Jobin Yvon) spectrofluorimeter with a resolution of 2 nm.

The emission decay curves were obtained by pulsed excitation with a laser radiation at 532 nm and recorded with a GaAs PMT (Hamamatsu) and a 500 MHz oscilloscope (Le Croy Waverunner, mod. LT342). All the spectroscopy measurements were carried out at room temperature.

Computational details

Complete active space self-consistent field (CASSCF) energy level calculations of Eu^{3+} ions in different defective sites (*i.e.*, with O_h and C_{3v} symmetry) were performed using the ORCA software, version 5.0.3.[37–39] The models were built exchanging Ba^{2+} with a Eu^{3+} ion in a BaF$_2$ crystalline cell, starting from the experimental CIF file[40] and without further structure optimization. The active space involves seven 4f orbitals and the six Eu^{3+} valence electrons (*i.e.*, CASSCF(6,7)), while contributions from states of different multiplicity (*i.e.*, quintets, triplets and singlets) were considered in the calculation through the state averaged (SA) approach. To consider relativistic effects, the scalar relativistic Douglas–Kroll–Hess (DKH) Hamiltonian and the spin–orbit coupling (SOC) operator were employed, including its second order DKH transformation. SARC2-DKH-QZVP[41] and DKH-DEF2-TZVP[42] basis sets were respectively employed for Eu^{3+} and F$^-$, while Ba^{2+} cations were treated as 2+ point charges through the effective core potential (ECP) approach.[43]

Results and discussion

An MOCVD approach has been successfully used for the fabrication of undoped BaF$_2$ and Eu-doped BaF$_2$ thin films on Si (100) and quartz substrates, using a multicomponent mixture of second generation β-diketonate precursors consisting of Ba(hfa)$_2$·tetraglyme and Eu(hfa)$_3$·diglyme mixed in 0.99:0.01 molar ratio. Due to the similar nature of the ligands, these precursors act as a single molten source by providing all the necessary elements (Ba, Eu and F) for the formation of the Eu-doped BaF$_2$ phase.

In order to compare the thermal performance of the mixture and the individual precursors, Fig. 1 shows the TGA curves of the single fluorinated β-diketonate precursors of barium and europium along with the 1:0.2 (Ba:Eu) mixture of the same precursors. The graph shows that the weight loss of the mixture as a function of temperature follows the same trend as the least volatile compound, namely Ba(hfa)$_2$·tetraglyme, leaving a residue of less than 10%.

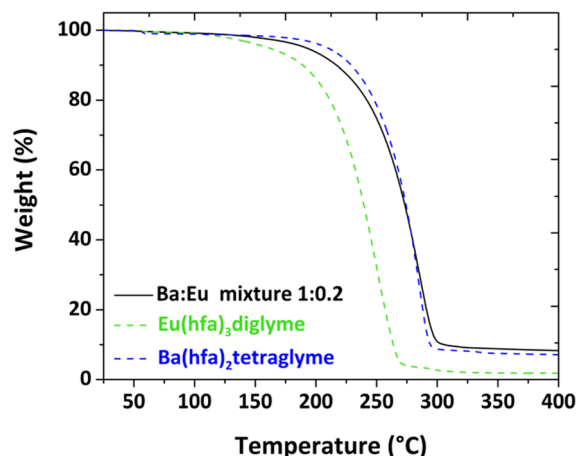Fig. 1 TGA curves of the Ba(hfa)$_2$·tetraglyme and Eu(hfa)$_3$·diglyme single precursors and the Ba(hfa)$_2$·tetraglyme : Eu(hfa)$_3$·diglyme 1 : 0.2 mixture.

Preliminary deposition studies have been done on silicon substrates to verify the purity, homogeneity, and correct stoichiometry of the films. In order to investigate the influence of temperature on the structure, morphology and DC properties of Eu-doped BaF$_2$ thin films, samples have been fabricated by changing the deposition temperature from 300 to 600 °C. Deposition rates were also estimated from FE-SEM cross-sectional measurements at each temperature. The structural properties of the deposited films were studied by XRD analysis. Fig. 2 illustrates the XRD patterns of Eu-doped BaF$_2$ thin films deposited on silicon substrates at various temperatures and compared with a typical pattern of an undoped BaF$_2$ film deposited at 400 °C.

The diffraction patterns of the analyzed samples show the formation of polycrystalline BaF$_2$ single phase for all the thin films deposited in the 300–600 °C temperature range. In fact, the patterns present diffraction peaks at 2θ values of 25.00°,
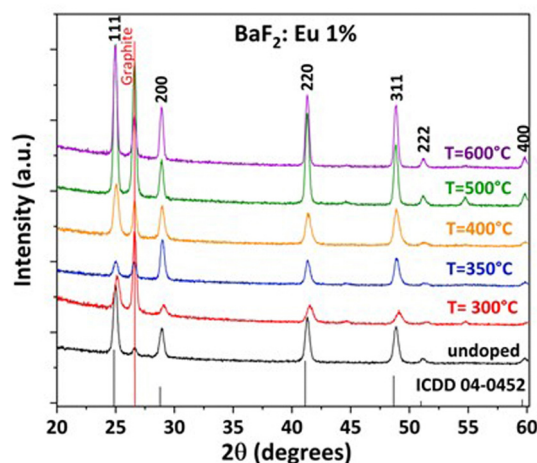

Fig. 2 XRD patterns of the undoped BaF$_2$ films deposited at 400 °C (black line) on Si and BaF$_2$: Eu (1%) at 300 °C (red line), 350 °C (blue line), 400 °C (yellow line), 500 °C (green line), and 600 °C (purple line) on Si. Graphite has been added as an internal standard.

This journal is © The Royal Society of Chemistry 2023

J. Mater. Chem. C, 2023, **11**, 12195–12205 | **12197**

28.92°, 41.30°, 48.84°, 51.18°, and 59.82° corresponding, respectively, to the characteristic 111, 200, 220, 311, 222 and 400 reflections of the BaF_2 cubic phase (International Centre for Diffraction Data, ICDD, database no. 04-0452). The relative intensities of peaks in these patterns mainly correspond to those reported in the ICDD database, indicating that there is no preferential direction growth. The a-cell parameter for a BaF_2 cubic structure was calculated by using graphite as internal standard and the relationship between d_{hkl} and a lattice parameter. In the case of the Eu-doped BaF_2 thin films fabricated at different temperatures (300–600 °C), the a-axis cell parameter is 6.16 (7) Å, while for the undoped one the a-axis cell parameter is equal to 6.17 (5) Å. The value of the undoped film is smaller than the theoretical a-axis cell parameter of 6.200 Å (ICDD no. 85-1342), indicating the presence of compressive strain. To our knowledge, no data are available in the literature for the a-axis cell parameter of BaF_2 deposited films. The slight reduction of the a lattice parameter for the doped BaF_2 samples is due to the introduction, in substitutional positions, of the trivalent Eu^{3+} ion, which has a smaller ionic radius (1.20 Å in 8-coordination) than the divalent barium ion (1.42 Å in 8-coordination).[23]

On the other hand, the effect of charge difference between Eu^{3+} and Ba^{2+} ions is compensated by the formation of cation vacancies, the formation of fluoride clusters and/or the presence of interstitial fluorine within the structure.[44,45] This phenomenon was recently demonstrated by the group of Pellegrino *et al.* who evaluated the effect of CaF_2 structure distortion following the insertion of trivalent Ln ions.[21] Therefore, it is expected that an increase of concentration of the dopant ions inside the crystalline structure would produce a shift of the diffraction reflections at even higher 2θ values.

Interestingly, in the present study, the variation of deposition temperature has no evident effect on the diffraction peak positions (Fig. 1), while it can be noted that the peak intensities tend to increase as the deposition temperature is increased, which can be ascribed on the one hand to a higher crystallinity degree, and on the other hand, to an increase of the film thickness up to 500 °C deposition temperature, as also confirmed by the FE-SEM images (see below).

On varying the Eu doping concentrations, as expected, the patterns show a predictable tendency of shifting diffraction peaks to higher values of two theta as the dopant concentration increases.

By extrapolation of the a-axis cell parameter of the doped samples with various amounts of europium, a decreasing trend of the a-axis cell is evident due to the shift of diffraction peaks to higher angles, with values of the parameter going from 6.17(5) for the undoped BaF_2 to 6.14 (5) for the 20% doped BaF_2 film (Fig. 3). The a-axis cell values of the differently doped films are reported in the table of Fig. 3.

Quantitative EDX analysis has been carried out to establish the composition of the films in terms of Eu^{3+} ion concentration and to exclude the presence of impurities. Since the percentage of europium (nominal concentration of $Eu(hfa)_3$·diglyme at 1% with respect to $Ba(hfa)_2$·tetraglyme) in the samples is difficult to measure because of the EDX detection limit, additional Eu-doped BaF_2 films
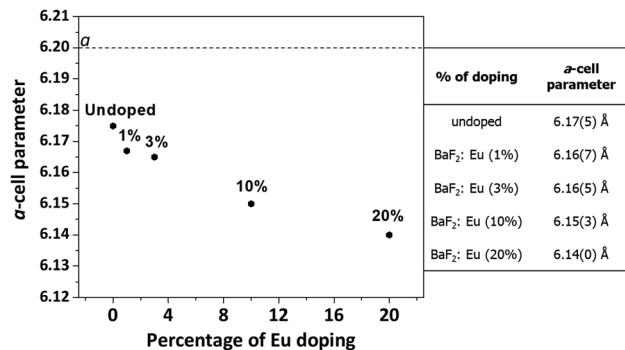

% of doping	a-cell parameter
undoped	6.17(5) Å
BaF_2: Eu (1%)	6.16(7) Å
BaF_2: Eu (3%)	6.16(5) Å
BaF_2: Eu (10%)	6.15(3) Å
BaF_2: Eu (20%)	6.14(0) Å

Fig. 3 a-axis parameter variation of the BaF_2 films as a function of the Eu doping amount. The dotted line indicates the theoretical value of 6.200 Å.

with a higher concentration of Eu^{3+} (nominal concentration at 10%) were deposited at 400 °C, in order to evaluate the elemental composition of the film. The EDX spectrum (Fig. S2, ESI†) shows the Ba L lines in the 4.3–5.2 keV range, the F Kα peak at 0.65 keV and the Eu L lines in the 5.5–6.4 keV range. The quantitative analysis confirms a good match between the nominal concentration of the precursor starting mixture, *i.e.* 0.9 $Ba(hfa)_2$·tetraglyme:0.1 $Eu(hfa)_3$·diglyme, and the EDX quantitative analysis, which yields the following amounts of about 0.9 Ba:0.1 Eu in the film. Furthermore, no O or C peaks are detected (K_α peaks should appear at 0.525 keV and at 0.277 keV, respectively), thus confirming the presence of a pure barium fluoride phase without impurities.

The morphology of the BaF_2 thin films was investigated through FE-SEM analysis. The FE-SEM images of Eu-doped BaF_2 thin films deposited on Si (100) substrates in the 300–600 °C temperature range are shown in Fig. 4.

For samples deposited at various temperatures, the surfaces look homogeneous and compact over the whole area (1 cm × 1 cm). In Fig. 4(a), the sample deposited at 300 °C presents a very smooth surface with quite small-sized grains, while the
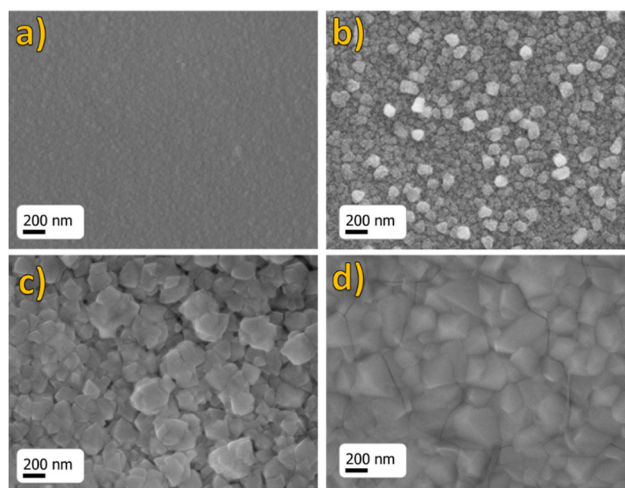

Fig. 4 FE-SEM images of BaF_2:Eu (1%) films prepared by MOCVD on an Si substrate at deposition temperatures of (a) 300 °C, (b) 400 °C, (c) 500 °C and (d) 600 °C.

12198 | *J. Mater. Chem. C*, 2023, **11**, 12195–12205

This journal is © The Royal Society of Chemistry 2023

films deposited at 400 °C (Fig. 4(b)) present, instead, a compact surface with grains appearing quite irregular in shape and size, of the order of 80 nm. However, when the deposition temperature becomes higher, the grain dimensions increase up to 200–300 nm, as seen in samples deposited at 500 °C (Fig. 4(c)). Furthermore, the sample deposited at the highest temperature of 600 °C (Fig. 4(d)) shows slightly bigger grains up to 400 nm with a well-defined crystalline habit. However, some cracking on the surface is barely visible at this higher temperature. This effect is likely due to the considerable difference between thermal expansion coefficients of the BaF_2 film and silicon substrate (BaF_2: 18.1×10^{-6} °C^{-1} vs. Si: 2.6×10^{-6} °C^{-1} at 273 K).

Fig. 5 shows a comprehensive overview of cross-sectional images of BaF_2: Eu (1%) on films deposited on Si substrates at increasing deposition temperatures. The cross-sections indicate a thickness of 180 ± 30 nm for sample deposited at 300 °C (Fig. 5(a)), 1.93 ± 0.03 μm for films deposited at 400 °C (Fig. 5(b)), 1.91 ± 0.03 μm and 1.43 ± 0.03 μm for samples deposited at 500 °C and 600 °C (Fig. 5(c) and (d)), respectively. Therefore, this behavior points to a clear dependence of film thickness on the deposition temperature. Accordingly, it is possible to calculate the film growth rate (reported in Table S2, ESI†) for films prepared at different temperatures and perform a kinetic study on the MOCVD deposition process of BaF_2 films.

The Arrhenius plot of ln (growth rate) vs. $1000/T$ for films deposited on Si substrates from 300 °C to 600 °C is shown in Fig. 6. From the Arrhenius plot, two different growth regimes are evident. From 300 °C to 400 °C, the film growth rate increases exponentially with temperature, according to the Arrhenius law. In this temperature range, the BaF_2 growth rate is strongly influenced by the substrate temperature and the type of growth is under kinetic control. A growth rate of about 32 nm min^{-1} is found at 400 °C. Thus, the decomposition of the precursors on the substrate surface can be considered the rate determining step. The activation energy for this first region, calculated from the straight line's slope of Fig. 6, is equal to 77 ± 14 J K^{-1} mol^{-1}.

Fig. 6 Arrhenius Plot for Eu-doped BaF_2 films grown through MOCVD.

From 400 °C to 600 °C, instead, a positive slope is derived, from which a negative activation energy is obtained, indicating that, in this deposition temperature range, BaF_2 film growth occurs in the mass transport-limited regime, since no dependency of the growth rate on the surface temperature is observed.

Finally, an EDX line mapping investigation has been carried out to assess the vertical compositional homogeneity of the Eu doped BaF_2 samples.

The intensities of the Ba L lines and the Eu L lines are remarkably constant throughout the thickness under consideration, as can be observed in Fig. 7 for the 20% Eu-doped sample. This indicates that there is no stratification or segregation of the doping element in the film, thus confirming a compositional homogeneity both on the surface and along the entire thickness of the film.

As a representative example, the room temperature excitation spectrum of the Eu^{3+} doped BaF_2 thin film prepared at 600 °C is shown in Fig. 8. The excitation bands are typical of the Eu^{3+} ion, in good agreement with those found for similar fluoride hosts.[46] In particular, the spectrum is dominated by a quite narrow excitation band peaked at 394 nm, due to the $^7F_0 \rightarrow {}^5L_6$ transition of the Eu^{3+} ion. Moreover, other less intense bands are present in the spectrum, due to transitions from the ground state to several excited energy levels of the Eu^{3+} ions.
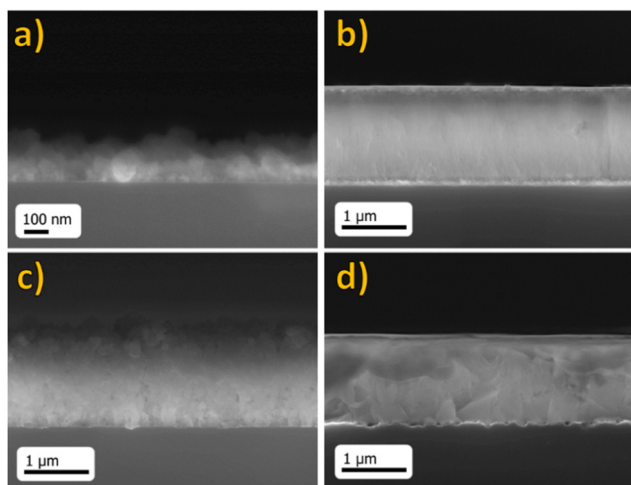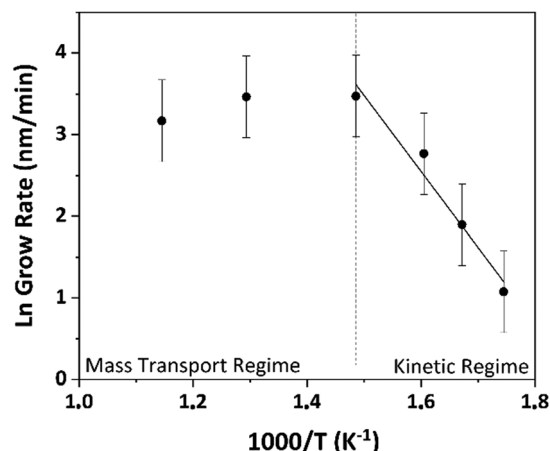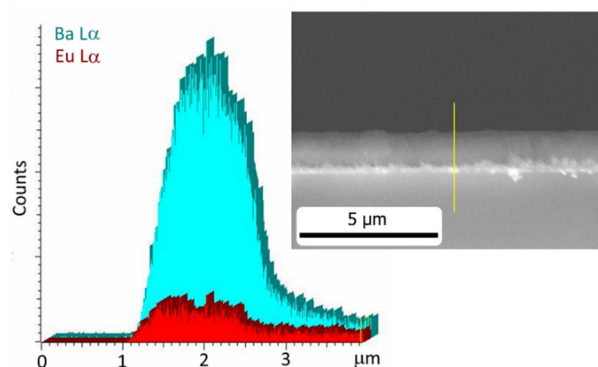

Fig. 5 FE-SEM cross-sectional images of Eu-doped BaF_2 film on Si at deposition temperatures of (a) 300 °C, (b) 400 °C, (c) 500 °C and (d) 600 °C.

Fig. 7 EDX line mapping of the BaF_2:Eu (20%) cross-sectional sample.

This journal is © The Royal Society of Chemistry 2023

J. Mater. Chem. C, 2023, 11, 12195–12205 | 12199
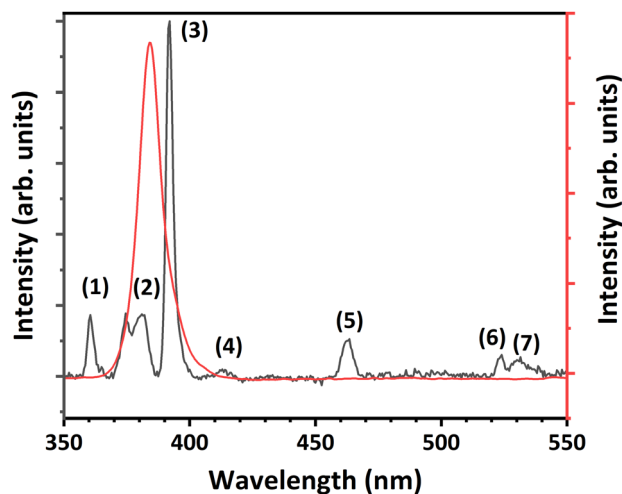
Fig. 8 Black line: room temperature excitation spectrum (λ_{em} = 613 nm) of the Eu^{3+} doped BaF_2 thin film grown at 600 °C. The energy levels involved in the transitions are indicated as $^7F_0 \to {}^5D_4$ (1), $^5G_{2-6}$ (2), $^5L_6$ (3), $^5D_3$ (4), $^5D_2$ (5), $^5D_1$ (6); and $^7F_1 \to {}^5D_1$ (7). Red line: emission spectrum of the used UV LED lamp.

It is worth noting that a weak band around 530 nm is present, due to the $^7F_1 \to {}^5D_1$ transition.

In fact, the population of the $^7F_1$ energy level (N_1) from which this transition starts, can be obtained according to the Boltzmann distribution law:

$$\frac{N_1}{N_0} = e^{-\frac{\Delta E}{k_B T}} \tag{1}$$

where N_0 represents the $^7F_0$ ground state population, k_B the Boltzmann constant and T the absolute temperature.

From the excitation spectrum shown in Fig. 8, the $^7F_0 \to {}^5D_1$ and $^7F_1 \to {}^5D_1$ excitation bands have been fitted with Gaussian profiles and their barycenters are found to be at 523.4 ± 0.2 nm (19 106 ± 7 cm^{-1}) and 531.5 ± 0.5 nm (18 815 ± 17 cm^{-1}), respectively. Therefore, the energy gap between the $^7F_0$ and $^7F_1$ energy levels is estimated to be 290 ± 30 cm^{-1}. For this energy gap, assuming that the population of the $^7F_2$ energy level is negligible at room temperature with respect to the sum of $^7F_0$ and $^7F_1$ energy level populations, from eqn (1) the $^7F_1/^7F_0$ population ratio is found to be 0.25 at room temperature, indicating that if the laser radiation is properly tuned, transitions starting from the $^7F_1$ level are possible and can contribute to populate the ^5D_J excited energy levels. Moreover, in Fig. 8 the emission spectrum of the used UV LED flashlight has been shown (red line).

By comparing the Eu^{3+} ion excitation spectrum and the emission spectrum of the flashlight, it can be noted that the exciting source can be considered as multi-wavelength radiation, able to efficiently excite the Eu^{3+} ions. In fact, from Fig. 8, it can be noted that the stronger Eu^{3+} excitation bands, indicated as (2) and (3) in Fig. 8, are located in the near UV region from 350 to 400 nm, well inside the radiation emitted from our LED flashlight.

The luminescence spectra of Eu-doped BaF_2 thin films grown at different temperatures are shown in Fig. 9. The emission bands are due to transitions of the Eu^{3+} ions, decaying radiatively from the $^5D_0$ excited level to the lower lying ^7F_J (J = 0, 1, 2, 3, 4) ones.

All the samples show excellent emission intensities, as demonstrated by the observed high signal to noise ratios.

For the sake of clarity, the energy level schemes of Eu^{3+} ions in the BaF_2 host, in O_h and C_{3v} symmetry sites, have been shown in Fig. 10, taken from Jouart et al.[47,48]

From the emission spectra, it can be noted that the features of the emission bands are different on changing the deposition temperature. Of great significance are the emission bands in the 580–600 nm (17 240–16 667 cm^{-1}) range, due to $^5D_0 \to {}^7F_1$ magnetic dipole transitions that are poorly dependent on the local environment around the lanthanide ions.[49] Differently, the bands in the 610–630 nm (16 393–15 873 cm^{-1}) region are due to $^5D_0 \to {}^7F_2$ electric dipole transitions that are allowed only for lanthanide sites without inversion symmetry, and they are very sensitive to local symmetry.
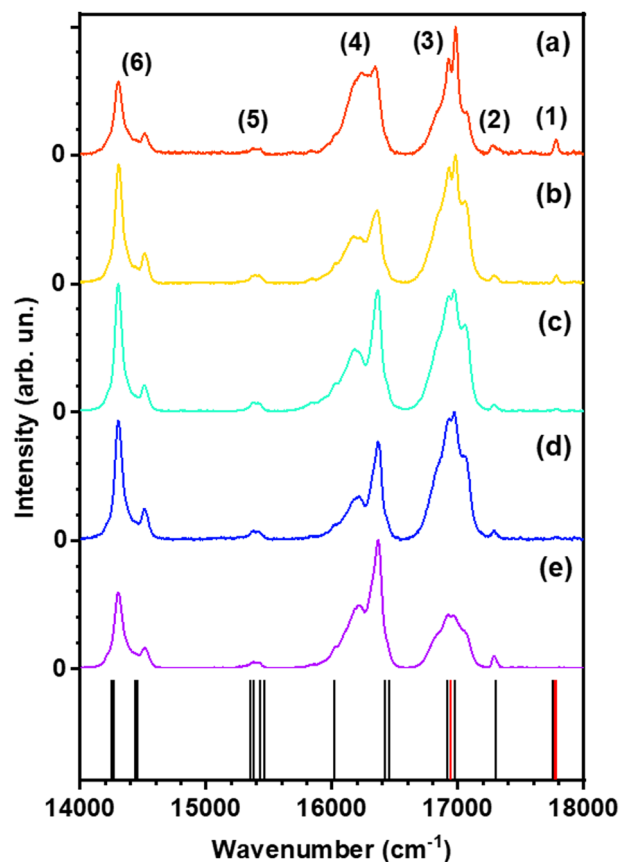

Fig. 9 Room temperature emission spectra of Eu doped (1%) BaF_2 thin films (λ_{exc} = 385 nm) on Si (100) support, at different deposition temperatures: (a) 600 °C; (b) 500 °C; (c) 400 °C; (d) 350 °C; and (e) 300 °C. Transition assignments for emission bands: (1) $^5D_1 \to {}^7F_2$; (2) $^5D_0 \to {}^7F_0$; (3) $^5D_0 \to {}^7F_1$; (4) $^5D_0 \to {}^7F_2$; (5) $^5D_0 \to {}^7F_3$; and (6) $^5D_0 \to {}^7F_4$. Energy transitions calculated for Eu^{3+} ions in C_{3v} (black bars) and O_h (red bars) local symmetry (from ref. 47 and 48).

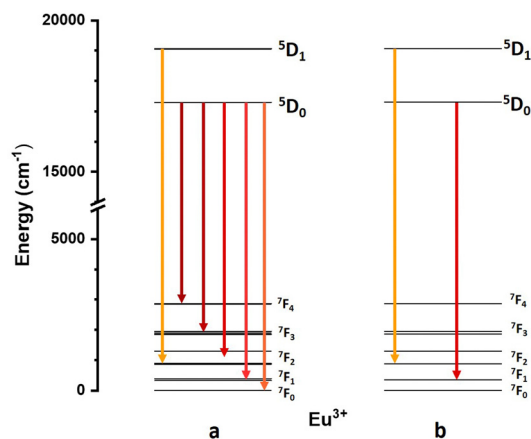12200 | J. Mater. Chem. C, 2023, 11, 12195–12205

This journal is © The Royal Society of Chemistry 2023

Fig. 10 Energy level schemes of Eu^{3+} ions in the BaF_2 host, in C_{3v} (a) and O_h (b) symmetry sites (from ref. 47 and 48). Arrows represents the observed emission transitions.

The asymmetry ratio R, defined as

$$R = \frac{I(^5D_0 \rightarrow {}^7F_2)}{I(^5D_0 \rightarrow {}^7F_1)} \quad (2)$$

where I represents the integrated area of the $^5D_0 \rightarrow {}^7F_J$ ($J = 1, 2$) transitions, depends on the symmetry of the site in which the lanthanide ion is accommodated.[50]

From the observed emission spectra, it is clear that for the sample deposited at 300 °C (see Fig. 9(e)) the intensity ratio of the two emission bands in the 610–630 nm (16 393–15 873 cm^{-1}) and 580–600 nm (17 240–16 667 cm^{-1}) range, due to the $^5D_0 \rightarrow {}^7F_2$ and $^5D_0 \rightarrow {}^7F_1$ transitions, respectively, is much higher (around 2) than those observed for the emission spectra for samples deposited at higher temperatures, for which R is less than 1.3 (see Fig. 9(a)–(d)).

Interestingly, this behavior suggests that, on average, the Eu^{3+} ions in the BaF_2 sample deposited at 300 °C are in a less symmetric environment, which is compatible with a slightly lower crystallinity degree with respect to other samples prepared at higher temperatures.

These results are also in agreement with those found from the XRD analysis (Fig. 2). The lower symmetry for the sample prepared at the lowest temperature could therefore be due to a higher number of defects, and this observation indicates that the defect amount decreases in the lattice structure with increasing deposition temperature, due to the higher crystallinity degree. This behavior agrees with the results obtained by Sharma *et al.*, who investigated the spectroscopic properties of Eu^{3+} doped BaF_2 nanoparticles[13] heat treated at different temperatures (from 400 to 800 °C) and found that the Eu^{3+} ions are in a more asymmetric environment in the sample treated at lower temperatures.

The specific nature of the sites in which the Eu^{3+} ions are accommodated was investigated through site-selective laser spectroscopy.[47,48] Generally, Eu^{3+} in doped fluorite-type crystals is located in cubic sites with O_h symmetry, *i.e.* with a bivalent cation being replaced and a charge-compensating F^- ion

distant from the Eu^{3+}, (see Fig. S3a, ESI†) which is the case for BaF_2 when co-doped with a small amount of NaF.[53]

Additionally, a trigonal site with C_{3v} symmetry has been identified,[47,51] where a compensating F^- ion is located in the $(\frac{1}{2}, \frac{1}{2}, \frac{1}{2})$ next-nearest-neighbor (NNN) interstitial position (see Fig. S3b, ESI†). This arrangement causes the energy levels of the lanthanide ions to split into several components, in particular in two components for both the $^7F_1$ and $^7F_2$ multiplets, which is the most common situation for very low Eu^{3+} concentrations in the BaF_2 host (0.03 mol%).[42] For higher Eu^{3+} concentrations (around 1 mol%) other emission lines were also observed, attributed to different local environments of the lanthanide, tentatively also proposed for pairs of nearest neighbors (NN) or NNN Eu^{3+} ions.

To corroborate these findings, we conducted *ab initio* multi-reference SA-CASSCF calculations on Eu-doped BaF_2 models featuring O_h and C_{3v} symmetry (see Fig. S3c and d, respectively, ESI†). Remarkably, such models are strongly ionic due to the presence of several unbalanced F^- anions, but this should not influence the energy levels of Eu^{3+} in a considerable way, while the coordination around the lanthanide does.[52,53] Evaluation of the ^7F_J ($J = 0$–6) energies in the two cases, compared with the available experimental data from Jouart *et al.*,[47,48] is reported in Table 1. The calculated energies follow the trend of the experimental data, showing a good agreement (*i.e.*, within ±100 cm^{-1}) in all cases but the $^7F_2$ levels, for which the discrepancy is up to almost 200 cm^{-1}. Some information on the location of Eu^{3+} ions can also be inferred from the profile detail of the emission bands of the measured spectra. As a general observation, the emissions starting from the different Stark levels are strongly overlapped, mainly due to homogeneous (*i.e.*, thermal) and inhomogeneous (*i.e.*, local disorder around the lanthanide ion) broadening. The good agreement between the theoretical and experimental data of the ^7F_J level energies makes it possible to compare the presently observed transitions with those previously reported by Jouart *et al.* in relation to different sites.[47,48] To clearly show the presence of Eu^{3+} in different sites in our samples, in Fig. 9 we report, along with the emission spectra, the $^5D_0 \rightarrow {}^7F_J$ ($J = 0$–5) and $^5D_1 \rightarrow {}^7F_2$ transition energies taken from the literature,[47] with black and red bars referring to transitions between energy levels in trigonal (C_{3v}) and cubic (O_h) symmetry, respectively. To do this, we analyzed the emission bands due to the $^5D_0 \rightarrow {}^7F_1$ magnetic dipole transition, for which emission contributions deriving from Eu^{3+} ions accommodated both in C_{3v} and O_h sites are expected.
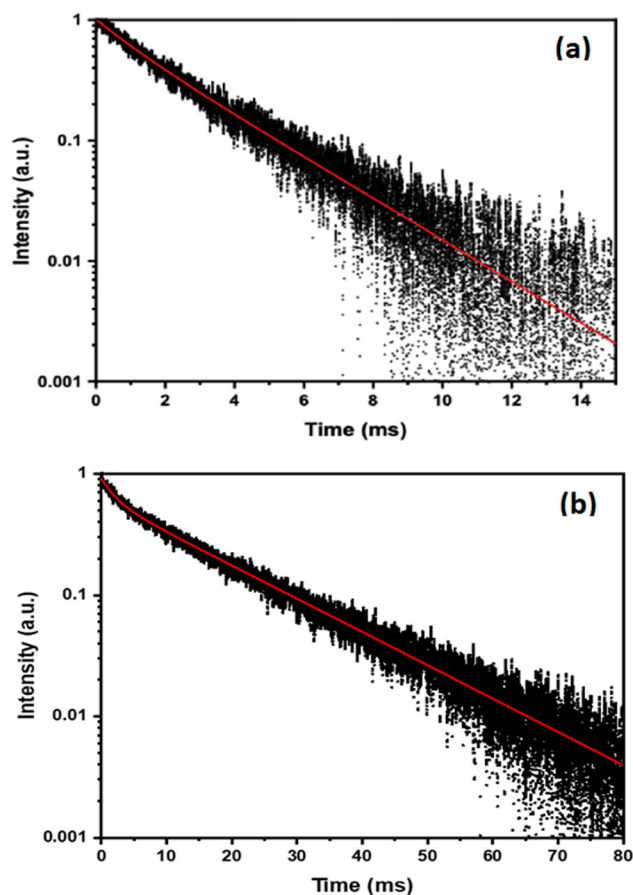
In this case, the two expected $^5D_0 \rightarrow {}^7F_1$ transitions for Eu^{3+} ions in BaF_2 in the C_{3v} symmetry site found by Jouart *et al.*[47] and peaked at 16 975 and 16 910 cm^{-1}, at a measurement temperature of 77 K, are in very good agreement with our measurements, thus suggesting that contributions from the Eu^{3+} ions in C_{3v} symmetry is remarkable for our samples. On the other hand, energy gaps of 17 304 cm^{-1} and 16 956 cm^{-1} between the $^5D_0$ and $^7F_0$ or $^7F_1$ Stark energy sublevels of Eu^{3+} ions in cubic center (O_h),[48] respectively, have been estimated, which were hardly recognized in the present investigation. Thus, the latter contribution to the $^5D_0 \rightarrow {}^7F_1$ emission transitions is probably low, since the respective band (around 16 700–17 200 cm^{-1})

This journal is © The Royal Society of Chemistry 2023

J. Mater. Chem. C, 2023, **11**, 12195–12205 | **12201**

Table 1 Theoretical (Th) and experimental (Exp) ^7F_J (J = 0–6) energy levels (in cm^{-1}) of Eu^{3+} in cubic (O_h) and trigonal (C_{3v}) symmetric sites, with the appropriate number of degenerate states (n) and energy difference (Δ) between Exp and Th, considering the average value of all the ^7F_J states (for a specific J value) when more energy levels are available. States with similar energies (within 0.2 cm^{-1}) are reported as degenerate

	O_h				C_{3v}			
	Exp[48]	Th	n	Δ	Exp[47]	Th	n	Δ
$^7F_0$	0	0.0	1		0	0	1	
$^7F_1$	348	366.1	3	−18.1	327	343.7	2	−16.7
					392	414.8	1	−22.8
$^7F_2$	869	990.6	3	−121.6	859	977.5	2	−118.5
	1283	1087.7	2	195.3	884	1014.9	1	−130.9
					1290	1094.2	2	195.8
$^7F_3$	1865	1899.5	3	−34.5	1845	1890.8	2	−45.8
	1938	1902.0	3	19.3	1877	1906.1	2	−29.1
		1968.7	1		1924	1910.9	2	13.1
					1950	1974.1	1	−24.1
$^7F_4$	2857	2765.7	1		2850	2767.7	1	82.3
		2902.4	3		2869	2900.7	1	
		2970.2	3	−74.3		2906.4	2	
		2999.3	2			2967.5	1	−85.8
						2975.7	2	
						3003.2	2	
$^7F_5$	—	3970.3	3		3789	3969.6	3	
		4038.8	3			4035.7	2	
		4101.5	2			4041.2	1	
		4102.3	3			4083.9	1	
						4106.6	2	
						4125.8	2	
$^7F_6$	—	5184.0	1		—	5149.6	1	
		5197.8	3			5163.9	2	
		5205.4	3			5196.1	2	
		5277.2	2			5230.7	1	
		5279.4	3			5238.4	1	
		5283.7	1			5284.4	2	
						5298.2	2	
						5304.6	1	
						5306.8	1	

Fig. 11 Room temperature emission decays of Eu doped (1%) BaF$_2$ thin films (λ_{exc} = 532 nm) on the Si (100) support, at 600 °C deposition temperature: (a) λ_{em} = 612 nm, $^5D_0 \rightarrow {}^7F_2$ transition and (b) λ_{em} = 589 nm, $^5D_0 \rightarrow {}^7F_1$ transition.

shows a very broad profile without prominent features. Moreover, it should be underlined that the emission spectra could also feature contributions from Eu^{3+} ions located in other sites[47] and/or from vibronic transitions, particularly important at room temperature,[54] as well as bands derived from Eu^{3+} clustering, i.e. pairs of NN or NNN Eu^{3+} ions, as observed in doped CaF$_2$[55] and BaF$_2$ hosts.[56] Remarkably, a weak but clearly detected emission band is observed at 562.4 ± 0.3 nm (17 781 ± 9 cm^{-1}), attributed to a transition between the $^5D_1$ and $^7F_2$ levels of the Eu^{3+} ions. Notably, the wavelength position of this band is in perfect agreement with that by Jouart et al.[47] (562.7 nm, 17 771 cm^{-1}), assigned to a transition of Eu^{3+} ions in a C_{3v} center. From the emission spectra, it can be noted that the intensity of this band increases on increasing the deposition temperature. Since the $^5D_1$ emission is strongly quenched by cross-relaxation processes between two Eu^{3+} ions[47] the observed behavior suggests the presence of clustering of the Eu^{3+} ions for samples prepared at the lowest temperature. On increasing the deposition temperature, the emission intensity of the band from the $^5D_1$ level increases, indicating that the Eu^{3+} ions tend to separate, therefore decreasing the cross-relaxation processes.

In order to gain more information about the sites where the Eu^{3+} ions are accommodated, room temperature emission decay curves were also measured for the Eu doped (1%) BaF$_2$ thin film sample deposited at 600 °C on Si (100) by monitoring emissions at 612 nm (16 340 cm^{-1}) and at 589 nm (16 978 cm^{-1}), attributed to $^5D_0 \rightarrow {}^7F_2$ and $^5D_0 \rightarrow {}^7F_1$ transitions, respectively. The measured emission decay curves are shown in Fig. 11.

The emission decays were fitted using a multiexponential curve, defined as:

$$I = \sum_i A_i \exp\left(-\frac{t}{\tau_i}\right) \tag{3}$$

where A_i and τ_i represent the weight and decay time of the i-th contribution, while I is the total emission intensity.

The intensity-weighted average lifetime τ_{avg} is defined as:[57]

$$\tau_{avg} = \sum_i \frac{A_i \tau_i^2}{A_i \tau_i} \tag{4}$$

The emission decays measured at 612 and 589 nm were fitted with a biexponential curve (see eqn (3)) and the values of weights, decay times and intensity-weighted average lifetime are reported in Table 2. It is worth noting that the obtained τ_{avg} value, 2.36 ms, for the emission at 612 nm (due to the $^5D_0 \rightarrow {}^7F_2$ transition) is similar to the value (1.80 ms) found at room

Table 2 Decay times, weights and intensity-weighted average lifetimes obtained by fit of the Eu^{3+} emission decay curves for the BaF_2 thin film sample grown at 600 °C

Emission wavelength (nm)	τ_1 (ms)	A_1	τ_2 (ms)	A_2	τ_{avg} (ms)
612 nm	0.97 ± 0.03	$22\% \pm 2\%$	2.520 ± 0.015	$78\% \pm 2\%$	2.36 ± 0.03
589 nm	2.073 ± 0.015	$31.6\% \pm 0.1\%$	15.81 ± 0.02	$68.4\% \pm 0.1\%$	15.03 ± 0.02

temperature from the same emission wavelength by Wang et al.[58] for Eu^{3+} doped BaF_2 microcrystals, prepared by a hydrothermal technique. Of notable interest, the τ_{avg} value obtained in the present investigation for the emission at 589 nm (due to the $^5D_0 \rightarrow {}^7F_1$ transition) is much longer than the value found for the 612 emission (see Table 2). This behavior indicates that contributions to the emission intensity from different sites are present in the decay curves. In fact, this indicates that Eu^{3+} sites with relatively high symmetry, probably close to cubic, can generate emission intensity mainly around 589 nm, as highly symmetric sites allow mainly $^5D_0 \rightarrow {}^7F_1$ magnetic dipole transitions. Moreover, these highly symmetric sites do not contribute to the emission at a wavelength around 612 nm, as for them the $^5D_0 \rightarrow {}^7F_2$ electric dipole transitions are almost completely forbidden. The τ_{avg} value found at room temperature in the present study for emission at 589 nm, which is 15.03 ms, is much longer than those found by other authors for the same fluoride nanocrystals in different systems, as nanocrystalline BaF_2:Eu^{3+} glass-ceramic materials,[59] with an average lifetime of around 3.4 ms, or Eu^{3+} doped nanoparticles prepared by the ionic liquid-assisted solvothermal method,[13] with average lifetimes depending on the experimental conditions, ranging from 1.15 to 5.61 ms at room temperature. This behavior suggests that for the sample deposited at the highest temperature (600 °C) a significant fraction of the luminescent Eu^{3+} ions are accommodated in sites with high symmetry, tentatively attributed to site close to cubic symmetry (see Fig. S3, ESI†). Nonetheless, other experimental evidence involving site selection spectroscopy would be needed to confirm this hypothesis, but this is outside of the scope of this study.

Conclusions

An extensive study has been conducted on the production of europium doped BaF_2 thin films for use in energy conversion. In order to have an easily scalable process and strong control over the composition, microstructure, and morphology of the films, an MOCVD approach is proposed. The chemical composition of the films has been tuned by changing the composition of the precursor mixture in order to tailor the useful Eu amount to optimize the luminescence properties. The diffraction patterns show that polycrystalline BaF_2 phase films are produced in the 300 to 600 °C temperature range, with peak intensities that tend to increase with the increasing deposition temperature. These phenomena can be attributed to both an increase in film thickness and a higher degree of crystallinity. Additionally, the peak positions are strictly related to the dopant %, with a shift toward higher angle with increasing Eu^{3+} ion concentrations, thus resulting in a decrease of the lattice parameter, an

effect due to the replacement of larger Ba^{2+} ions by the smaller Eu^{3+} ions. The morphology, investigated through FE-SEM analysis is impacted by temperature, particularly as the deposition temperature increases, grain dimension tends to rise up until 400 nm, as it is observed in samples deposited at 600 °C. Film growth rates as high as 32 nm min^{-1} have been found in the deposition range of 400–500 °C.

The prepared thin films show a strong Stokes luminescence under excitation in the excited levels of Eu^{3+} ions. The profile of the emission bands depends on the deposition temperature, indicating that the local environment of the lanthanide ions is slightly different. The sample prepared at the lowest temperature reveals that the Eu^{3+} ions are accommodated in sites of lower symmetry with respect to the samples prepared at other temperatures, most probably due to a higher number of defects. The defect amount decreases in the lattice structure with increasing deposition temperature. Analysis of the emission decay curves reveals that a relevant number of Eu^{3+} ions with quite high symmetry is present. The simulation of the energy levels of the ^7F_J ($J = 0$–6) multiplets for the Eu^{3+} ions in different site geometries, calculated by CASSCF methods, indicates that the calculated energy levels agree with those extracted from experimental data.

These MOCVD grown Eu-doped BaF_2 films are very promising for applications as downshifting layers in photovoltaic cells to exploit the UV component of the solar spectrum.

Conflicts of interest

There are no conflicts to declare.

Acknowledgements

This journal is © The Royal Society of Chemistry 2023

J. Mater. Chem. C, 2023, **11**, 12195–12205 | **12203**

experimental setups. The authors also acknowledge the Computational Platform of the Information Systems and Technology Direction of the University of Verona, Italy.

Notes and references

1 G. W. Crabtree and N. S. Lewis, *Phys. Today*, 2007, **60**, 37–42.

2 NREL. Best Research-Cell Efficiency. (2020).

3 X. Huang, S. Han, W. Huang and X. Liu, *Chem. Soc. Rev.*, 2013, **42**, 173–201.

4 D. Yang, H. Liang, Y. Liu, M. Hou, L. Kan, Y. Yang and Z. Zanga, *Dalton Trans.*, 2020, **49**, 4725–4731.

5 H. T. Kim, K. Lee, W. Jin, H. D. Um, M. Lee, E. Hwang, T. H. Kwon and K. Seo, *Sci. Rep.*, 2018, **8**, 16974.

6 J. C. Bünzli and A. S. Chauvin, *Chapter 261 – Lanthanides in Solar Energy Conversion. in Including Actinides, Elservier*, 2014, vol. 44, pp. 169–281.

7 J. C. G. Bünzli and S. V. Eliseeva, *Chem. Sci.*, 2013, **4**, 1939–1949.

8 G. Lucchini, A. Speghini, P. Canton, F. Vetrone and M. Quintanilla, *Nanoscale Adv.*, 2019, **1**, 757.

9 N. Kumam, L. P. Singh, K. Srivastava and N. R. Singh, *J. Lumin.*, 2018, **203**, 59–66.

10 N. U. Rahman, W. U. Khan, S. Khan, X. Chen, J. Khan, J. Zhao, Z. Yang, M. Wu and Z. Chi, *J. Mater. Chem. A*, 2019, **7**, 6467–6474.

11 M. Ran, N. Liu, H. Y. Yang, R. Meng, M. Chen, H. Lu and Y. Yang, *Appl. Phys. Lett.*, 2020, **116**, 113503.

12 R. N. Grass and W. J. Stark, *Chem. Commun.*, 2005, 1767–1769.

13 R. K. Sharma, S. Nigam, Y. N. Chouryal, S. Nema, S. P. Bera, Y. Bhargava and P. Ghosh, *ACS Appl. Nano Mater.*, 2019, **2**, 927–936.

14 E. Palo, L. Pihlgren, M. Tuomisto, T. Laihinen, I. Hyppanen, J. Kankare, M. Lastusaari, T. Soukka, H. C. Swart and J. Holsa, *Opt. Mater.*, 2016, **59**, 49–54.

15 V. Kale, M. Lastusaari, J. Holsa and T. Soukka, *RSC Adv.*, 2015, **5**, 35858–35865.

16 M. R. Catalano, A. L. Pellegrino, P. Rossi, P. Paoli, P. Cortelletti, M. Pedroni, A. Speghini and G. Malandrino, *New J. Chem.*, 2017, **41**, 4771–4775.

17 A. L. Pellegrino, M. R. Catalano, P. Cortelletti, G. Lucchini, A. Speghini and G. Malandrino, *Photochem. Photobiol. Sci.*, 2018, **17**, 1239–1246.

18 X. Zhang, Z. Zhao, X. Zhang, D. B. Cordes, B. Weeks, B. Qiu, K. Madanan, D. Sardar and J. Chaudhur, *Nano Res.*, 2015, **8**, 636–648.

19 A. L. Pellegrino, P. Cortelletti, M. Pedroni, A. Speghini and G. Malandrino, *Adv. Mater. Interfaces*, 2017, **4**, 1–6.

20 A. L. Pellegrino, G. Lucchini, A. Speghini and G. Malandrino, *J. Mater. Res.*, 2020, **35**, 2950–2966.

21 A. L. Pellegrino, S. La Manna, A. Bartasyte, P. Cortelletti, G. Lucchini, A. Speghini and G. Malandrino, *J. Mater. Chem. C*, 2020, **8**, 3865–3877.

22 S. Balabhadra, M. F. Reid, V. Golovko and J. R. Wells, *J. Alloys Compd.*, 2020, **834**, 155165.

23 E. I. Madirov, V. A. Konyushkin, A. N. Nakladov, P. P. Fedorov, T. Bergfeldt, D. Busko, I. A. Howard, B. S. Richards, S. V. Kuznetsov and A. Turshatov, *J. Mater. Chem. C*, 2021, **9**, 3493–3503.

24 J. R. Wells and R. J. Reeves, *J. Lumin.*, 1996, **66–67**, 219–223.

25 W. Drozdowski and A. J. Wojtowicz, *J. Alloys Compd.*, 2000, **300–301**, 261–266.

26 M. Heise, G. Scholz, T. Krahl and E. Kemnitz, *Solid State Sci.*, 2019, **91**, 113–118.

27 B. Ritter, P. Haida, F. Fink, T. Krahl, K. Gawlitza, K. Rurack, G. Scholz and E. Kemnitz, *Dalton Trans.*, 2017, **46**, 2925–2936.

28 C. Lorbeer, J. Cybinska, E. Zych and A.-V. Mudring, *Opt. Mater.*, 2011, **34**, 336–340.

29 I. G. Neizvestny, D. V. Ishchenko, I. O. Akhundov, S. P. Suprun and O. E. Tereshchenko, *Dokl. Phys.*, 2020, **65**, 15–17.

30 X. M. Fang, T. Chatterjee and P. J. McCann, *J. Vac. Sci. Technol., B*, 1996, **14**, 2267–2270.

31 P. S. Kirlin, R. Binder, D. R. Winn, J. O'Hare, C. LaPierre and M. Whitmore, *Nucl. Instrum. Methods Phys. Res., Sect. A*, 1990, **289**, 261–264.

32 M. L. Hitchman, S. H. Shamlian, D. D. Gilliland, D. J. Cole-Hamilton, J. A. P. Nash, S. C. Thompson and S. L. Cook, *J. Mater. Chem.*, 1995, **5**, 47–52.

33 A. P. Purdy, A. D. Berry, R. T. Holm, M. Fatemi and D. K. Gaskill, *Inorg. Chem.*, 1989, **28**, 2799–2803.

34 H. Sato and S. Sugawara, *Inorg. Chem.*, 1993, **32**, 1941–1945.

35 G. Malandrino, F. Castelli and I. L. Fragalà, *Inorg. Chim. Acta*, 1994, **224**, 203–207.

36 G. Malandrino and I. L. Fragalà, *Coord. Chem. Rev.*, 2006, **250**, 1605–1620.

37 F. Neese, *Wiley Interdiscip. Rev.: Comput. Mol. Sci.*, 2012, **2**, 73–78.

38 F. Neese, *Wiley Interdiscip. Rev.: Comput. Mol. Sci.*, 2022, **12**, e1606.

39 F. Neese, F. Wennmohs, U. Becker and C. Riplinger, *J. Chem. Phys.*, 2020, **152**(22), 224108.

40 H. E. Swanson and E. Tatge, Standard X-ray diffraction powder patterns, National Bureau of Standards Circular (U.S.), *Circular*, 1953, **539**(1), 1–95.

41 D. Aravena, F. Neese and D. A. Pantazis, *J. Chem. Theory Comput.*, 2016, **12**(3), 1148–1156.

42 F. Weigend and R. Ahlrichs, *Phys. Chem. Chem. Phys.*, 2005, **7**, 3297–3305.

43 M. Kaupp, P. v R. Schleyer, H. Stoll and H. Preuss, *J. Chem. Phys.*, 1991, **94**(2), 1360–1366.

44 F. Ma, F. Su, R. Zhou, Y. Ou, L. Xie, C. Liu, D. Jiang, Z. Zhang, Q. Wu, L. Su and H. Liang, *Mater. Res. Bull.*, 2020, **125**, 110788.

45 D. Chen and Y. Wang, *Nanoscale*, 2013, **5**, 4621–4637.

46 P. Cortelletti, M. Pedroni, F. Boschi, S. Pin, P. Ghigna, P. Canton, F. Vetrone and A. Speghini, *Cryst. Growth Des.*, 2018, **18**, 686–694.

47 J. P. Jouart, C. Bissieux and G. Mary, *J. Lumin.*, 1987, **37**(3), 159–165.

48 J. P. Jouart, M. Bouffard, G. Klein and G. Mary, *J. Lumin.*, 1991, **50**(5), 273–277.

12204 | *J. Mater. Chem. C*, 2023, **11**, 12195–12205

This journal is © The Royal Society of Chemistry 2023

49 R. D. Peacock, The intensities of lanthanide f ↔ f transitions, *Rare Earths. Structure and Bonding*, Springer, Berlin, Heidelberg, 1975, p. 22.

50 A. M. Srivastava, M. G. Brik, W. W. Beers and W. Cohen, *Opt. Mater.*, 2021, 110931.

51 J. P. R. Wells, *Laser spectroscopy of alkaline earth fluoride crystals doped with trivalent samarium and europium ions*, University of Canterbury. Physics and Astronomy, 1996.

52 D. Aravena, M. Atanasov and F. Neese, *Inorg. Chem.*, 2016, **55**(9), 4457–4469.

53 L. Babetto, S. Carlotto, A. Carlotto, M. Rancan, G. Bottaro, L. Armelao and M. Casarin, *Inorg. Chem.*, 2021, **60**(1), 315–324.

54 P. A. Tanner, *Chem. Soc. Rev.*, 2013, **42**, 5090.

55 S. Renard, P. Camy, A. Braud, J. L. Doualan and R. Moncorgé, *J. Alloys Compd.*, 2008, **451**(1–2), 71–73.

56 E. I. Madirov, V. A. Konyushkin, A. N. Nakladov, P. P. Fedorov, T. Bergfeldt, D. Busko, I. A. Howard, B. S. Richards, S. V. Kuznetsov and A. Turshatov, *J. Mater. Chem. C*, 2021, **9**, 3493.

57 Y. Li, S. Natakorn, Y. Chen, M. Safar, M. Cunningham, J. Tian and D. D. Li, *Front. Phys.*, 2020, **8**, 576862.

58 X. Wang, Y. Bu, Y. Xiao, C. Kan, D. Lu and X. Yan, *J. Mater. Chem. C*, 2013, **1**, 3158–3166.

59 N. Pawlik, B. Szpikowska-Sroka, J. Pisarska, T. Goryczka and W. A. Pisarski, *Materials*, 2019, **12**, 3735.

This journal is © The Royal Society of Chemistry 2023

J. Mater. Chem. C, 2023, **11**, 12195–12205 | **12205**